1

Guided Wave Interaction in Photonic Integrated Circuits — A Hybrid Analytical / Numerical Approach to Coupled Mode Theory

Manfred Hammer

Theoretical Electrical Engineering, University of Paderborn,
Warburger Straße 100, 33098 Paderborn, Germany
manfred.hammer@uni-paderborn.de

Abstract. Computational tools are indispensable in the field of photonic integrated circuits, for specific design tasks as well as for more fundamental investigations. Difficulties arise from the usually very limited range of applicability of purely analytical models, and from the frequently prohibitive effort required for rigorous numerical simulations. Hence we pursue an intermediate strategy. Typically, an optical integrated circuit consists of combinations of elements (waveguide channels, cavities) the simulation and design of which is reasonably well established, usually through more or less mature numerical solvers. What remains is to predict quantitatively the interaction of the waves (modes) supported by these elements. We address this task by a quite general, "Hybrid" variant (HCMT) of a technique known as Coupled Mode Theory. Using methods from the realm of finite-element numerics, the optical properties of a circuit are approximated by superpositions of eigen-solutions for its constituents, leading to good quantitative, computationally low-dimensional, and easily interpretable models. This chapter describes the theoretical background of the HCMT approach, explains its limitations, hints at implementational details, and discusses a series of examples that illustrate the versatility of the technique.

1.1 Introduction

A certain class of photonic / integrated optical devices is distinguished by the following common feature: The optical electromagnetic field can be described adequately by the propagation and interaction of a few known, or conveniently computable, basic fields. Traditionally these are the local guided modes supported by the waveguide channels that constitute the optical circuit. By superimposing the basis modes with coefficient functions that vary along the associated propagation coordinate, it is then in many cases straightforward to write a plausible ansatz for the total optical field. After suitable projection, e.g. using "reciprocity properties" [1], or via variational restriction [1], one obtains — necessarily approximate — differential equations for

the amplitudes of the constituting fields. Approaches of this kind are usually labelled "coupled mode theory" (CMT); we refer to [2–4], and to the textbooks [1, 5–7] for overviews of the variety of existing formulations. Figure 1.1 gives a schematic impression, in a context of examples, some of which will be discussed later in this chapter.

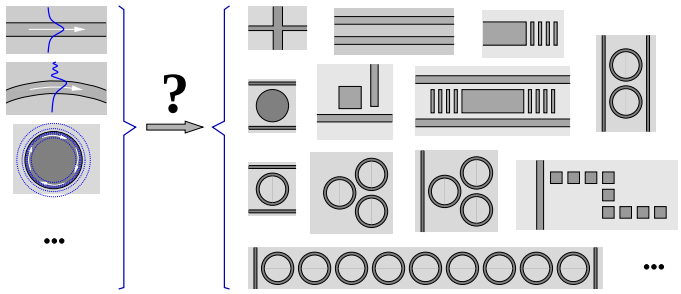

Fig. 1.1. Coupled mode theory, schematically: Known constituting fields (left) serve to predict the optical properties of composite circuits (right). Many other combinations (. . .) of constituents and / or circuits are conceivable, which lend themselves to coupled mode modelling.

The conventional CMT equations permit explicit analytical solutions only in special situations, typically for longitudinally homogeneous systems comprised of a few waveguides. For other configurations one obtains systems of differential equations with non-constant coefficients, or coupled systems of higher dimensions, that require numerical means for their solution. In all cases the interaction of the basic fields can be examined by inspecting the evolution of CMT amplitudes, given either through explicit expressions, or as a numerical representation of the amplitude evolutions.

According to the collection of "selected papers on coupled-mode theory in guided-wave optics" [4] (SPIE Milestone Series, 1993), the existing methods for linear structures can be classified by the terms "codirectional" CMT, covering the unidirectional guided light propagation along closely spaced, more or less parallel waveguide cores, and "contradirectional" CMT, which concerns the waves in corrugated channels (waveguide gratings). As all these techniques rely on a common *spatial* propagation coordinate, and relate to the frequency domain Maxwell equations, one might denote them as "spatial CMT" or "frequency domain CMT". Note that the requirement of this common propagation coordinate, although successful, appears to be decidedly unnatural in some instances, e.g. in the case of optical microring resonators coupled to straight waveguides [8, 9].

With intensifying interest in optical cavities in the late 1990s (the keyword "cavity" is not being mentioned in the index of [4]), a variant of coupled mode theory was proposed for the field of waveguide optics, where *time* plays the role of the propagation coordinate [10], to be denoted as "coupled modes in time" or "time domain CMT". Emphasis here is in the modelling of systems of coupled cavities, and the

exploration of optical filter functionalities that might be realizable with these systems [11–14]. Localized resonances serve as basis fields; waveguide channels are taken into account merely as power outlets. Coupling coefficients can be calculated explicitly, in principle, by means of power balance argument from their counterparts in a frequency-domain-CMT-description [11].

In particular this later time-domain CMT variant, but also the former spatial CMT, are frequently seen to be used as "mere" phenomenological models. Certain quantities in the equations are not rigorously linked to Maxwell's equations, to the basis fields whose interaction is discussed, nor to the underlying structure, i.e. coupling coefficients are treated as fit-parameters.

Despite the attractiveness to obtain efficient, interpretable, and quantitative low-dimensional models, when it comes to *ab initio*[1] simulations of 3-D real-life devices, the techniques are seemingly hardly ever applied in a rigorous way. A few instances are found in [15–17] (codirectional CMT applied to configurations with several multimode channels; guided wave interaction in anisotropic, magnetooptic waveguides), [18,19] (CMT for the interaction between photonic crystal waveguides and optical fibers, extreme refractive index contrasts), and [20] (bent and straight channels, horizontal and vertical coupling, fully vectorial). This is the more remarkable as methods to calculate the basis fields, mode solvers for dielectric optical channels [21,22], and / or solvers for the resonant eigenmodes of optical cavities, are part of several commercial packages for simulations in photonics / electrodynamics (cf. e.g. [23–26]). The quite general approach as outlined in this chapter can be expected to constitute a straightforward extension of these mode solver packages, in principle.

1.1.1 Hybrid analytical / numerical coupled mode theory

A motivation can be found in the unification of the formerly different, partly distinct formulations of the variants of CMT. To this end we restrict the discussion exclusively to the frequency domain, and we *give up the notion of a common propagation coordinate*, and consequently of differential coupled mode equations. Instead, the coupled amplitudes, each a function of the respective modes' own "natural" propagation coordinate, are being discretized through 1-D finite elements. Localized resonances can enter with single unknown coefficients. Then a variational (Galerkin) procedure is applied that leads to a dense, but small-size, linear system of equations, which is solved numerically for the modal amplitudes. The possibility to inspect their functional behaviour is thus preserved. The name "Hybrid analytical / numerical" CMT (HCMT) refers to the analytical, low dimensional (i.e. involving few unknowns) modelling of the problems in terms of superpositions of known basis modes, and to the numerical procedures that are employed to discretize any unknown functions and to solve the resulting systems.

[1] The term *ab initio* is here used to indicate simulations that predict the optical electromagnetic field for given structural data (geometry, material properties, and excitation, if applicable), without any further fit parameters.

The approach has been proposed in [27] for a series of circuits with rectangular refractive index distributions, including a crossing of perpendicular waveguide channels, a waveguide-Bragg reflector, and systems of coupled square microcavities [27,28]. HCMT models of composite micro-ring or -disk circuits, based on either the bend modes supported by curved channels or interfaces, or on the whispering-gallery modes of entire circular cavities, have been discussed in [29,30]. Section 1.2 reviews the abstract theory. Prototypes for the constituting elements are introduced, followed by an outline of the generic solution procedure, and a discussion of implementational details. A series of 2-D examples with increasing complexity has been selected for Section 1.3, to highlight different aspects of the theoretical approach, and to provide benchmarks. Section 1.4 concludes with a few remarks on the (ongoing) implementation in 3-D.

1.2 Theoretical background

The homogeneous Maxwell equations in the frequency domain are considered, for the optical electric field $\boldsymbol{E}$ and magnetic field $\boldsymbol{H}$:

$$\boldsymbol{\nabla} \times \boldsymbol{H} - \mathrm{i}\omega\epsilon_0\epsilon\boldsymbol{E} = 0\,, \qquad -\boldsymbol{\nabla} \times \boldsymbol{E} - \mathrm{i}\omega\mu_0\boldsymbol{H} = 0\,. \tag{1.1}$$

Both fields oscillate $\sim \exp(\mathrm{i}\omega t)$ with angular frequency $\omega = k\mathrm{c} = 2\pi\mathrm{c}/\lambda$, specified by the vacuum wavelength λ, for vacuum wavenumber $k = 2\pi/\lambda$, vacuum speed of light c, vacuum permittivity ϵ_0, and vacuum permeability μ_0. We restrict the discussion to linear, lossless, and nonmagnetic dielectric media with relative permeability $\mu = 1$, spatially varying relative permittivity $\epsilon = n^2$, and refractive index n.

Given some specific scattering problem in the form of a refractive index distribution, wavelength parameter, and a specification of excitation conditions, some good idea about the internal working of the circuit forms the starting point for the HCMT analysis. One needs to identify the constituting elements that later establish the template for the overall field. Typically, these are the guided, or at least well confined, modes supported by the optical channels in the device, at the frequency in question, and / or some local resonances associated with any cavities in the device, in a frequency range of interest. We'll discuss typical examples in the following paragraphs. One needs to be aware that this field template determines the answers that can be expected from the model: One can, e.g., not expect information on radiative losses, if the template consists of lossless guided modes only. Obviously, these constituting fields need to be easily accessible, i.e. should be reliably computable (or be given, in 2-D, analytically). Computation of these modes requires, in turn, the specification of a permittivity distribution for a "part" of the total structure. In cases where that definition of a "separate" channel, or of an "individual" cavity is not obvious (cf., e.g., the discussion in [20]), one should select a permittivity function that satisfies the symmetry requirements for the respective modal analysis, and that is as *close as possible* to the permittivity of the full structure.

1.2.1 Straight waveguides

Figure 1.2 introduces a typical, schematic geometry for a straight waveguide channel. We look at one particular guided mode with vectorial profile $(\tilde{\boldsymbol{E}}, \tilde{\boldsymbol{H}})$ (this concerns all six — not necessarily nonzero — electric and magnetic field components), and real propagation constant β.

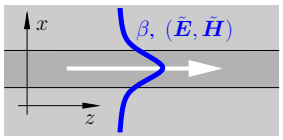

Fig. 1.2. Straight waveguide: A guided mode propagates along the longitudinal axis z, with propagation constant β and an electromagnetic profile $\tilde{\boldsymbol{E}}$, $\tilde{\boldsymbol{H}}$, that depends on the cross-section coordinates x, y.

If undisturbed, the mode propagates down the channel with an amplitude of constant magnitude. This relates to a field of the form

$$\boldsymbol{\psi}(x,y,z) = \begin{pmatrix} \tilde{\boldsymbol{E}} \\ \tilde{\boldsymbol{H}} \end{pmatrix}(x,y)\, \exp(-\mathrm{i}\beta z). \tag{1.2}$$

The presence of other parts of the circuit might change the magnitude and phase of the local amplitude. Hence we introduce an — at present unknown — function $f(z)$ of the "natural" propagation coordinate z of the mode. One thus assumes that the mode in question contributes to the overall electromagnetic field with a field of the form

$$\begin{pmatrix} \boldsymbol{E} \\ \boldsymbol{H} \end{pmatrix}(x,y,z) = f(z)\, \boldsymbol{\psi}(x,y,z). \tag{1.3}$$

At this point we switch to numerics. The primary unknown f is being discretized using finite elements. We outline briefly the most simple version of an equidistant discretization with 1-D elements of first order. By considering the positioning of the waveguide in the circuit, an interval $[z_0, z_N]$ has to be identified, outside of which the amplitude can be assumed to be constant, due to the absence of potential interaction with other fields. We divide that interval into N pieces of length $\Delta z = (z_N - z_0)/N$ each, with nodal points $z_j = z_0 + j\Delta z$. Piecewise linear element functions

$$\alpha_j(z) = \begin{cases} (z - z_{j-1})/\Delta z & \text{if } z_{j-1} \le z \le z_j, \\ (z_{j+1} - z)/\Delta z & \text{if } z_j \le z \le z_{j+1}, \\ 0 & \text{otherwise,} \end{cases} \quad \text{for } j = 0, \ldots, N, \tag{1.4}$$

are introduced, with the exceptions that $\alpha_0(z) = 1$ if $z \le z_0$, and $\alpha_N(z) = 1$ if $z_N \le z$. At the interior nodal points $j = 1, \ldots, N-1$, these are standard "triangle" functions with a support of length $2\,\Delta z$; the elements α_0 and α_N, with nodal points

at the boundaries of the computational interval, are constant with value 1 in the half-infinite exterior intervals. We expand the amplitude function into the elements as

$$f(z) = \sum_{j=0}^{N} f_j \, \alpha_j(z), \tag{1.5}$$

introducing the coefficients f_j as new, discrete, unknowns. The contribution of the particular mode of the straight waveguide has now been given the form

$$\begin{pmatrix} \boldsymbol{E} \\ \boldsymbol{H} \end{pmatrix}(x,y,z) = \sum_{j=0}^{N} f_j \, \left[\alpha_j(z) \, \boldsymbol{\psi}(x,y,z)\right]. \tag{1.6}$$

This template incorporates the "boundary conditions" for the present part of the problem, i.e. it shows the proper field behaviour in the exterior regions, where we assumed the interaction to vanish: The mode in question propagates with constant amplitude f_0 as an incoming field for $z < z_0$. Note that f_0 is actually a given quantity, specifying the external excitation of that particular mode. For $z > z_N$, (1.6) is a pure outgoing mode with amplitude f_N, which represents the — as of yet unknown — modal output of our channel.

Note that one expression of the form (1.6), with a separate set of discrete unknowns, and individual initial values, must be included into the overall template (1.13) for each individual mode that might become relevant. Typically this might concern modes of higher order, if supported by the waveguide in question, and modes of both directions of propagation (different signs of propagation constants, different signs of certain components of the vectorial mode profiles), if a bidirectional model is desired.

1.2.2 Bent channels, or curved interfaces

Bent channels are most conveniently described in polar / cylindrical coordinates. Figure 1.3 introduces a typical geometry, here with radius R. We consider one particular bend mode with vectorial electromagnetic profile $(\tilde{\boldsymbol{E}}, \tilde{\boldsymbol{H}})$ and angular propagation constant γ, i.e., a field of the form

$$\boldsymbol{\psi}(r,\theta,y) = \begin{pmatrix} \tilde{\boldsymbol{E}} \\ \tilde{\boldsymbol{H}} \end{pmatrix}(r,y) \, \exp(-\mathrm{i}\gamma R\theta). \tag{1.7}$$

For sufficiently small radius, and sufficiently large refractive index contrast, this could also concern a mode supported by the radially outermost interface only. Note that the definition of the bend radius R is, to some degree, arbitrary, and that it influences the value of the angular wavenumber γ [31].

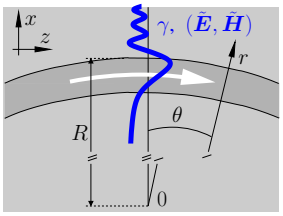

Fig. 1.3. A curved waveguide with radius R (outer rim). Cylindrical coordinates r, θ, y are introduced. A bend mode with profile $(\tilde{\boldsymbol{E}}, \tilde{\boldsymbol{H}})$, depending on the transverse coordinates r, y, propagates along the bend with complex angular propagation constant γ.

Suppose that the bend mode interacts with other parts of the circuit only weakly, such that it is a good approximation to assume that its contribution to the overall field is of the form

$$\begin{pmatrix} \boldsymbol{E} \\ \boldsymbol{H} \end{pmatrix}(r, \theta, y) = t(\theta)\, \boldsymbol{\psi}(r, \theta, y), \tag{1.8}$$

with an unknown amplitude t, here a function of the angular variable θ, the "natural" propagation coordinate of the bend mode.

Consider now a configuration [29] where a full 2π-length of the bend channel serves as a circular cavity. For the complex, in general non-integer, exponent γR, the mode field (1.7) exhibits a discontinuity at $\theta = 0, 2\pi$, which, in principle, could be compensated by an equally discontinuous amplitude function t. We prefer, however to remove the phase mismatch after one roundtrip, and the decay in amplitude, from the fixed part (1.7) of the template, by replacing the exponential term by an expression $\exp(-\mathrm{i}\kappa R\theta)$, with a real constant

$$\kappa = \mathrm{floor}(\mathrm{Re}\,\gamma R + 1/2)/R\,, \tag{1.9}$$

such that the integer number κR matches as closely as possible the angular phase gain of the bend mode. Here $\mathrm{floor}(x)$ is the largest integer smaller than x. Then, besides the interaction with other fields, the complex amplitude t also covers further phase variations, as well as the bend mode losses, both of which can be expected to be smooth at the transition $2\pi \to 0$.

Just as for the straight channel, the bend mode amplitude function $t(\theta)$ is now being discretized into 1-D finite elements, for the full circle $\theta \in [0, 2\pi]$, introducing discrete coefficients t_j. Expressions analogous to Eq. (1.4) apply, where the element functions $\alpha_j(\theta)$ with nodes at $\theta = 0$ and $\theta = 2\pi$ are identified. This implies that all coefficients are actual unknowns; the cavity is being excited through the interaction with other fields in the circuit. The contribution of the bend mode to the overall field is then of the form

$$\begin{pmatrix} \boldsymbol{E} \\ \boldsymbol{H} \end{pmatrix}(r, \theta, y) = \sum_j t_j\ [\alpha_j(\theta)\, \boldsymbol{\psi}(r, \theta, y)]\,. \tag{1.10}$$

Also here, for some particular bent channel, one might need to include more than one contribution of the form (1.10) in the overall template (1.13), e.g., to take bend modes of higher order into account, or to model bidirectional propagation.

1.2.3 Cavities

Our circuit might include pieces that support localized resonances. Typical examples are the whispering-gallery-modes (WGMs) of a circular cavity [30, 32] as in Figure 1.4. We focus on one of the eigenmodes with electromagnetic profile

$$\boldsymbol{\psi}(r,\theta,y) = \begin{pmatrix} \tilde{\boldsymbol{E}} \\ \tilde{\boldsymbol{H}} \end{pmatrix}(r,\theta,y) \tag{1.11}$$

and eigenfrequency ω^{c}, conventionally specified in terms of the resonance wavelength $\lambda_{\mathrm{r}} = 2\pi\mathrm{c}/\mathrm{Re}\,\omega^{\mathrm{c}}$, the Q-factor $Q = \mathrm{Re}\,\omega^{\mathrm{c}}/(2\mathrm{Im}\,\omega^{\mathrm{c}})$, and the ratio $\Delta\lambda = \lambda_{\mathrm{r}}/Q$, which corresponds to the linewidth (full-width at half maximum) of the outgoing radiation [33].

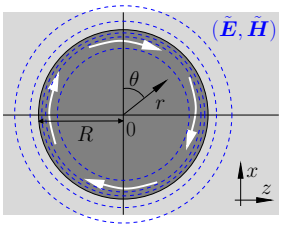

Fig. 1.4. A circular cavity with radius R supports a resonance with profile $(\tilde{\boldsymbol{E}},\tilde{\boldsymbol{H}})$, depending on the local cylindrical coordinates r,θ,y. The field oscillates in time with its own complex eigenfrequency.

The resonance can be expected to contribute significantly to our sought-after solution of Eqs. (1.1), if the real part of its complex eigenfrequency ω^{c} happens to be reasonably close to the given real angular frequency ω. Continuous-wave interaction with other parts of the circuit, at that frequency, will then excite the resonance with some amplitude c, unknown at present (note that this concerns stationary fields; transient effects are not covered by these models). We thus write a contribution to the overall field in the form of the mode profile (1.11), multiplied by the coefficient c:

$$\begin{pmatrix} \boldsymbol{E} \\ \boldsymbol{H} \end{pmatrix}(r,\theta,y) = c\,[\boldsymbol{\psi}(r,\theta,y)]\,. \tag{1.12}$$

As before, a separate expression, here with only one unknown each, needs to be written for each resonance that is to be included in the HCMT model. That might concern WGMs with a reversed direction of propagation, with close-by angular order, or modes of higher radial order.

1.2.4 Coupled mode field template

Depending on the positioning and orientation of any straight channels, bent channels, or cavities within the given circuit, the field templates (1.6), (1.10), and (1.12) are to be transformed from the previous local coordinates to the global system of the circuit. One observes that all these expressions are of the same form of a discrete sum over known fields, the terms in square brackets, with coefficients that are mostly unknown, and partly given, i.e. are related to external excitation. After the transformation, and after renaming the contributions, we thus obtain the following abstract, general field template in the form of a sum over "modal elements":

$$\begin{pmatrix} \boldsymbol{E} \\ \boldsymbol{H} \end{pmatrix}(x,y,z) = \sum_k a_k \begin{pmatrix} \boldsymbol{E}_k \\ \boldsymbol{H}_k \end{pmatrix}(x,y,z). \tag{1.13}$$

Here the index k runs over the finite element indices, for all modes, for all channels, and the resonances of all cavities in the model. The modal elements $(\boldsymbol{E}_k, \boldsymbol{H}_k)$, the terms in square brackets in (1.6), (1.10), and (1.12), combine the mode profiles, with related exponential dependences on the propagation coordinate, and the finite element functions, in case of a mode of a straight or bent channel. Any resonant fields serve directly as a modal element.

1.2.5 Projection & algebraic procedure

What remains to be determined are the unknown coefficients in the general expansion (1.13). We apply a procedure of Galerkin type [27, 30], borrowed from the realm of finite-element numerics. The Maxwell equations (1.1) are multiplied by trial fields $\boldsymbol{F}$, $\boldsymbol{G}$, and integrated over a suitable computational domain. This leads to a weak form of Eqs. (1.1). For reasons that become apparent in Section 1.2.7, it is here written as

$$\begin{aligned} &\iiint \mathcal{A}(\boldsymbol{F},\boldsymbol{G};\boldsymbol{E},\boldsymbol{H})\,\mathrm{d}x\,\mathrm{d}y\,\mathrm{d}z \\ -\,\omega &\iiint \mathcal{B}(\boldsymbol{F},\boldsymbol{G};\boldsymbol{E},\boldsymbol{H})\,\mathrm{d}x\,\mathrm{d}y\,\mathrm{d}z = 0 \quad \text{for all } \boldsymbol{F},\boldsymbol{G}, \end{aligned} \tag{1.14}$$

where

$$\mathcal{A}(\boldsymbol{F},\boldsymbol{G};\boldsymbol{E},\boldsymbol{H}) = \boldsymbol{F}^* \cdot (\boldsymbol{\nabla} \times \boldsymbol{H}) - \boldsymbol{G}^* \cdot (\boldsymbol{\nabla} \times \boldsymbol{E})\ , \tag{1.15}$$

$$\mathcal{B}(\boldsymbol{F},\boldsymbol{G};\boldsymbol{E},\boldsymbol{H}) = \mathrm{i}\epsilon_0\epsilon \boldsymbol{F}^* \cdot \boldsymbol{E} + \mathrm{i}\mu_0 \boldsymbol{G}^* \cdot \boldsymbol{H}\ . \tag{1.16}$$

Next we insert the generalized template (1.13) for $\boldsymbol{E}$, $\boldsymbol{H}$, and restrict Eq. (1.14) to the set of modal elements $(\boldsymbol{F},\boldsymbol{G}) \in \{(\boldsymbol{E}_k,\boldsymbol{H}_k)\}$. This leads to a system of linear equations of the form

$$\sum_k \left(A_{lk} - \omega B_{lk}\right) a_k = 0\,, \text{ for all } l \tag{1.17}$$

with "overlaps" of modal elements

$$A_{lk} = \iiint \mathcal{A}(\boldsymbol{E}_l, \boldsymbol{H}_l; \boldsymbol{E}_k, \boldsymbol{H}_k)\,\mathrm{d}x\,\mathrm{d}y\,\mathrm{d}z\,, \tag{1.18}$$

$$B_{lk} = \iiint \mathcal{B}(\boldsymbol{E}_l, \boldsymbol{H}_l; \boldsymbol{E}_k, \boldsymbol{H}_k)\,\mathrm{d}x\,\mathrm{d}y\,\mathrm{d}z\,. \tag{1.19}$$

In matrix form, with the coefficients a_k collected into a vector $\boldsymbol{a} = (\boldsymbol{u}, \boldsymbol{g})$, and ordered such that $\boldsymbol{u}$ represents the actual unknowns, while $\boldsymbol{g}$ corresponds to the given excitation, and with the matrix elements (1.18) arranged accordingly, the system (1.17) can be written

$$\left[\begin{pmatrix} \mathsf{A}_{\mathrm{uu}} & \mathsf{A}_{\mathrm{ug}} \\ \mathsf{A}_{\mathrm{gu}} & \mathsf{A}_{\mathrm{gg}} \end{pmatrix} - \omega \begin{pmatrix} \mathsf{B}_{\mathrm{uu}} & \mathsf{B}_{\mathrm{ug}} \\ \mathsf{B}_{\mathrm{gu}} & \mathsf{B}_{\mathrm{gg}} \end{pmatrix}\right] \begin{pmatrix} \boldsymbol{u} \\ \boldsymbol{g} \end{pmatrix} = 0\,, \quad \text{or} \tag{1.20}$$

$$\mathsf{K}_{\mathrm{u}}\boldsymbol{u} = -\mathsf{K}_{\mathrm{g}}\boldsymbol{g} \quad \text{with} \quad \mathsf{K}_{\mathrm{u}} = \begin{pmatrix} \mathsf{A}_{\mathrm{uu}} - \omega\mathsf{B}_{\mathrm{uu}} \\ \mathsf{A}_{\mathrm{gu}} - \omega\mathsf{B}_{\mathrm{gu}} \end{pmatrix}, \quad \mathsf{K}_{\mathrm{g}} = \begin{pmatrix} \mathsf{A}_{\mathrm{ug}} - \omega\mathsf{B}_{\mathrm{ug}} \\ \mathsf{A}_{\mathrm{gg}} - \omega\mathsf{B}_{\mathrm{gg}} \end{pmatrix}. \tag{1.21}$$

The matrix in Eq. (1.20) is square, thus the last system (1.21) is overdetermined. Hence we solve it in a least squares sense. One obtains, for given input $\boldsymbol{g}$, the response $\boldsymbol{u}$ at a prescribed excitation frequency ω as the solution of

$$\mathsf{K}_{\mathrm{u}}^{\dagger}\mathsf{K}_{\mathrm{u}}\boldsymbol{u} = -\mathsf{K}_{\mathrm{u}}^{\dagger}\mathsf{K}_{\mathrm{g}}\boldsymbol{g}\,. \tag{1.22}$$

Here the symbol † denotes the adjoint. The modal output amplitudes $\boldsymbol{u}$ are already the most interesting results, in many cases. The HCMT approximation to the full field can be obtained by substituting the values of $\boldsymbol{u}$ and $\boldsymbol{g}$, or $\boldsymbol{a}$, for the coefficients in Eqs. (1.13), or (1.6) (1.10) (1.12). Inspecting the respective amplitude functions (1.5) can give an impression of the interaction of the coupled modes.

1.2.6 Material dispersion & spectral scans

As this is a frequency domain method, incorporating material dispersion is straightforward, provided that suitable material models $\epsilon(\omega)$ are available. To evaluate the spectral properties of a device, one needs to repeat the former procedure for varying angular frequencies ω.

Frequently, however, one is interested in the response of a device on a narrow spectral range, with smooth material dispersion, but with the requirement to resolve fine spectral details, e.g. to adequately capture resonant features. Even for the 2-D case the computations can then become lengthy, where most of the effort is spent in repeatedly evaluating the modal element overlaps (1.18). A way out can be found by

observing that, for the given wavelength range, the properties of the basis fields, i.e. modal profile shapes and propagation constants / eigenfrequencies, and consequently the modal overlaps, change only moderately and smoothly, while any fine spectral features are due to the *solution* of the system (1.22). We then adopt the following strategy: The overlap matrices are evaluated for a few (2, 3) representative wavelengths, and stored. Only the solution of the (small sized) system (1.22), for *interpolated matrices*, is repeated for every wavelength sample. More explicit expressions can be found in [29]; this is observed to be an excellent approximation for the examples considered.

1.2.7 Eigenfrequencies of composite systems

For circuits that include optical cavities, one might be interested in a means to directly predict the spectral positions and widths of any resonances [30]. To this end one looks for — prospectively complex — values ω^{s} where the system

$$\boldsymbol{\nabla} \times \boldsymbol{H} - \mathrm{i}\omega^{\mathrm{s}}\epsilon_0\epsilon\boldsymbol{E} = 0, \quad -\boldsymbol{\nabla} \times \boldsymbol{E} - \mathrm{i}\omega^{\mathrm{s}}\mu_0\boldsymbol{H} = 0 \tag{1.23}$$

permits nonzero solutions $\boldsymbol{E}$, $\boldsymbol{H}$, subject to boundary conditions of outgoing waves only. As before, we look for approximate solutions in the form of the HCMT field template (1.13) for the specific configuration, now without any incoming waves. The unknown value ω^{s} replaces the former frequency parameter ω. One proceeds along the steps of Section 1.2.5 up to Eq. (1.20). Only the upper left quadrant of that equation remains relevant:

$$\mathsf{A}_{\mathrm{uu}}\boldsymbol{u} = \omega^{\mathrm{s}}\mathsf{B}_{\mathrm{uu}}\boldsymbol{u}. \tag{1.24}$$

Eq. (1.24) constitutes a generalized eigenvalue problem for pairs of eigenvectors $\boldsymbol{u}$ and eigenfrequencies ω^{s}. To distinguish the related fields from the basis fields that enter the template directly, we shall use the term "supermodes" for these resonances. One obtains a set of supermodes[2], each associated with a complex eigenfrequency ω^{s}, Q-factor $Q = \mathrm{Re}\,\omega^{\mathrm{s}}/(2\mathrm{Im}\,\omega^{\mathrm{s}})$, resonance wavelength $\lambda_{\mathrm{r}} = 2\pi\mathrm{c}/\mathrm{Re}\,\omega^{\mathrm{s}}$, linewidth $\Delta\lambda = \lambda_{\mathrm{r}}/Q$, and a supermode profile, which can be accessed by substituting the respective eigenvector into Eq. (1.13).

This type of analysis takes into account power outlets through bus waveguides if the CMT template includes the respective modes. The supermode Q-factors and linewidths then relate to the waves that the composite open cavity sends out through the access channels. Despite respective statements elsewhere [34], the present variant of CMT is well capable of evaluating these coupling-induced phase shifts with adequate accuracy. As an example, Figures 1.10, 1.13 show excellent agreement between the resonance wavelengths and linewidths associated with the supermodes,

[2] There are as many supermodes as there are unknowns in Eq. (1.24), in principle. The relevant ones need to be filtered out, typically by specifying a range of resonance frequencies, or a maximum level of attenuation.

and the peaks and dips in the spectral transmission curves. Note that, beyond observing that agreement, here we do not establish any formal relation between the scans of the transmission problem, and the supermode analysis. A means to do that could be to employ variational procedures again, in line with what has been carried out for 1-D problems in [35–37].

1.3 Numerical examples

The examples discussed in this section have been adapted from [27, 29, 30]. The list of other devices that have been modeled by means of the HCMT approach so far include waveguide-Bragg-reflectors and -filters [27], resonators with square cavities, and chains of these [27, 28], double-ring filters with parallel coupled rings [29], and a series of coupled-resonator optical waveguides (CROWs) with varying numbers of cavities [29, 30].

All of these are 2-D configurations, which have the advantage that — at least for numerical purposes — exact basis modes are available, and that benchmarking versus rigorous numerical or quasi-analytical methods is possible with reasonable effort. The equations given in Section 1.2 apply, with all y-dependences, derivatives with respect to y, and integrals over y-intervals omitted. Polarized solutions can be expressed in terms of the principal components E_y of TE-waves, and H_y of TM-waves. Note that this concerns comparably large model systems, borrowed from the realm of "classical" integrated optics / waveguide optics, not from "nanophotonics".

Partly with the intention to assess the validity of the method, we select parameters that refer to structures with substantial refractive index contrast. CMT approaches (at least the variant discussed here) certainly need not be restricted to "low contrast" configurations.

Our C++ -implementation relies on the routine libraries of [38, 39]. Rigorous quasi-analytical (quadri-directional eigenmode propagation, QUEP [38, 40], rectangular structures) or numerical solvers (finite-difference-time-domain, FDTD, commercial [23]; finite element method FEM, commercial [24]) have been used for benchmarking. For the fast computation of spectral HCMT data for Figures 1.10 and 1.13, the interpolation procedure as outlined in Section 1.2.6 [29] has been applied.

The modal element overlaps (1.18) are evaluated numerically by Gaussian quadrature [41], applied, as far as possible, piecewise in case of non-smooth fields at dielectric interfaces. For the templates that include bend modes (1.7) or localized resonances (1.11), the extension of the computational window must be suspected to be the most relevant among the computational parameters. For the example of Figure 1.10(a), enlarging the window from the original $(20\,\mu\mathrm{m})^2$ to $(45\,\mu\mathrm{m})^2$ leads to hardly any visible change of the transmission curves. The FEM-stepsizes of the discretized amplitude functions for modes of straight- and bent waveguides have

been selected such that the overall results, on the scale of the figures as given, appear to be converged.

1.3.1 Single waveguide

We start with a model of the single straight waveguide of Figure 1.5, intended as a check for consistency. There are potential alternative formulations with differences in the field template, or in the algebraic procedure (cf. the remarks in [1,27]), that do not work as the formalism adopted here. The CMT template is of the form Eq. (1.3), including the fundamental forward propagating mode only, with an input amplitude $f_0 = 1$, and with the amplitude function discretized over the range $z \in [-20, 20]\,\mu\text{m}$ at a stepsize $\Delta z = 2\,\mu\text{m}$. The computational window $z \in [< -20, > 20]\,\mu\text{m}$, $x \in [-3, 3]\,\mu\text{m}$ for evaluating the modal overlaps (1.18) covers the transverse mode profile extension sufficiently.

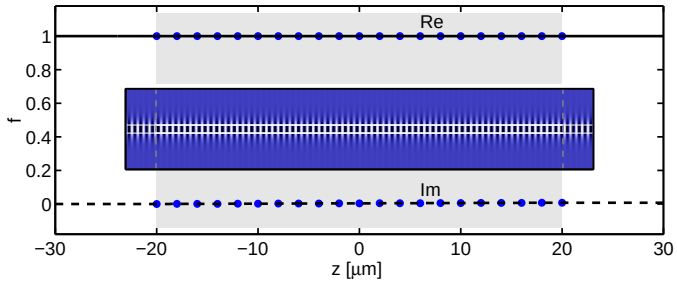

Fig. 1.5. A symmetric straight singlemode slab; complex HCMT amplitude f as a function of the propagation coordinate z. The inset shows a snapshot of the optical field, the principal component E_y of the TE polarized wave. Parameters: vacuum wavelength $\lambda = 1.55\,\mu\text{m}$, refractive indices 3.4 (core) and 1.45 (background), core thickness $0.2\,\mu\text{m}$. [27]

The present algorithm responds with the adequate constant amplitude, that relates to the unperturbed propagation of the modal wave along the channel. Note that the FE stepsize Δz is much larger than the wavelength of $\lambda/N_{\text{eff}} = 0.57\,\mu\text{m}$ associated with the mode with effective index $N_{\text{eff}} = 2.703$ (This same result can actually be achieved with a discretization of f into 2 elements only). In cases where the amplitude functions change only slowly along their respective coordinates, the modal elements cover the rapid oscillations of the optical fields, while the 1-D FE mesh only needs to resolve the slow variation of the amplitude.

1.3.2 Two straight parallel waveguides

Two parallel evanescently coupled waveguide cores constitute the "classical" CMT problem. Figure 1.6 introduces a corresponding structure. We use a HCMT template of the form

$$\begin{pmatrix} \boldsymbol{E} \\ \boldsymbol{H} \end{pmatrix}(x,y,z) = f_1(z)\,\boldsymbol{\psi}_1(x,y,z) + f_2(z)\,\boldsymbol{\psi}_2(x,y,z), \tag{1.25}$$

that includes the fundamental forward propagating modes $\boldsymbol{\psi}_1$, $\boldsymbol{\psi}_2$ of the separate cores, with their natural exponential dependence on z, as basis fields.

The amplitude functions f_1, f_2 are discretized over an interval $z \in [-20, 20]\,\mu\text{m}$ with a stepsize $\Delta z = 0.5\,\mu\text{m}$. We specify amplitudes $f_1(-20) = 1$, $f_2(-20) = 0$, i.e. all power is concentrated in waveguide (1) at the input. Due to the lateral mode overlap, constant mode amplitudes violate Eqs. (1.1), in contrast to the configuration of Section 1.3.1. Therefore here the computational window $z \in [-20, 20]\,\mu\text{m}$, $x \in [-3, 3]\,\mu\text{m}$ has to be restricted to the longitudinal FE interval. Figure 1.6 summarizes some results of the present model.

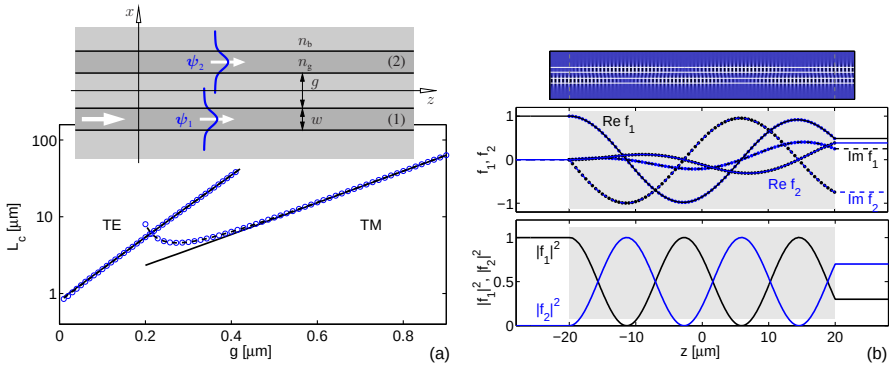

Fig. 1.6. Two coupled parallel waveguides. (a): coupling length L_c versus the gap width g. Continuous lines correspond to the exact length; circles indicate the present HCMT results; dashed lines (mostly shadowed by the HCMT data) are computed with a "conventional" CMT approach [1, 15]. TE and TM waves are considered. (b), for a gap $g = 0.25\,\mu\text{m}$, TE polarization: amplitude functions f_1 and f_2 for the fields associated with the the upper (index 2) and lower cores (index 1), real and imaginary parts (top) and absolute squares (bottom). The uppermost panel shows a time snapshot of the real, physical field. Parameters are as given for Figure 1.5: refractive indices $n_b = 1.45$, $n_g = 3.4$, core thickness $w = 0.2\,\mu\text{m}$, vacuum wavelength $\lambda = 1.55\,\mu\text{m}$. [27]

The HCMT model reproduces the well known periodic coupling process. The data for the half-beat or coupling length L_c is here determined as the distance between subsequent extrema in the z-dependence of $|f_1|^2$ and $|f_2|^2$, as shown for a particular

configuration in Figure 1.6(b). Panel (a) compares L_c, as a function of the coupler gap g, with exact values[3]. One finds excellent agreement for large gaps. More pronounced deviations are observed at narrower g for the less regular TM polarized fields (The derivatives of their principal magnetic components are discontinuous at the layer interfaces).

The plot also shows curves originating from "traditional" CMT analysis, i.e. relating to the solution of suitable differential coupled mode equations [1, 15]. These latter curves coincide almost perfectly with the present data. Hence, the HCMT approach described here provides directly a finite element solution of the differential equations that emerge in conventional CMT formulations.

1.3.3 Waveguide crossing

Given some experience with "traditional" CMT variants, one would hardly expect that some similar procedures could be applicable[4] to the waveguide crossing as introduced in Figure 1.7. For the present parameters, the horizontal channel supports one guided mode per polarization, while the vertical channel is multimode, depending on its width v.

For guided wave excitation in the horizontal channel, one expects the following behaviour: The input power will be partly reflected into the input channel, it will be partly transmitted to the outlet straight ahead, and part of the power will be carried upwards and downwards by one of the guided modes of the vertical core. Omitting any radiated fields[5], a plausible template for the global electromagnetic field includes bidirectional guided modes[6]of different orders, if applicable, for both the horizontal and the vertical channel:

$$\begin{pmatrix} \boldsymbol{E} \\ \boldsymbol{H} \end{pmatrix}(x,y,z) = f(z)\,\boldsymbol{\psi}^{\mathrm{f}}(x,y,z) + b(z)\,\boldsymbol{\psi}^{\mathrm{b}}(x,y,z) + \sum_m u_m(x)\,\boldsymbol{\psi}^{\mathrm{u}}_m(x,y,z) + \sum_m d_m(x)\,\boldsymbol{\psi}^{\mathrm{d}}_m(x,y,z). \quad (1.26)$$

[3] One regards the entire structure as one composite waveguide with three interior layers that supports, per polarization, two "supermodes" of different parity with slightly different propagation constants β_0 and β_1. These determine the coupling length as $L_c = \pi/|\beta_0 - \beta_1|$. The supermodes are computed by a solver (cf. e.g. [42]) for the modes of dielectric multilayer slabs.

[4] Certainly we do *not* intend to recommend the HCMT approach as the "method of choice" for this particular waveguide crossing.

[5] In special cases radiated fields can also be incorporated [27].

[6] Although the forward and backward propagating modes of the same channel share, up to the signs of certain field components identical profile shapes, the combination of electric and magnetic parts of the mode profile, as applied here, ensures orthogonality of the directional modes with respect to a suitable inner product [1, 43] ("power orthogonality").

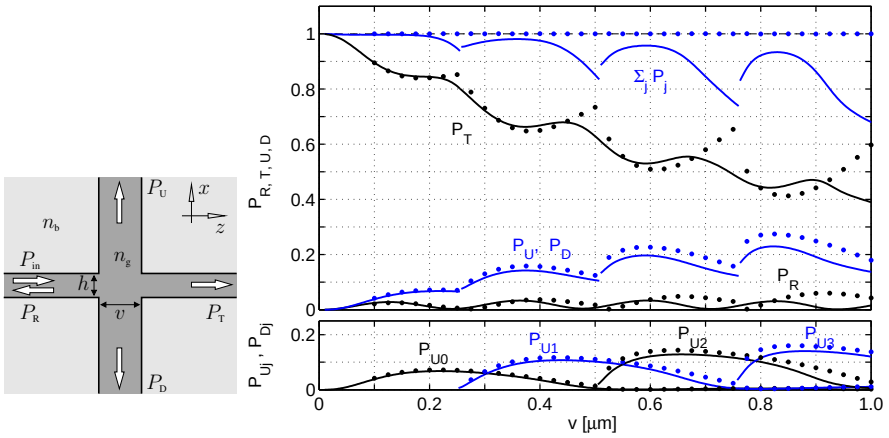

Fig. 1.7. Waveguide crossing: Guided power transmission versus the width v of the vertical core, HCMT results (dots) and QUEP simulations (lines, reference [40]). P_{R}, P_{U}, P_{T}, P_{D}, and $\sum_j P_j$ are the relative power carried by guided modes that leave the crossing through the left, upper, right, and lower channel, and the sum of these quantities, for unit excitation in the horizontal channel from the left. Lower panel: power fractions $P_{\mathrm{Um}} = P_{\mathrm{Dm}}$ associated with vertically outgoing guided modes of order $m = 0, 1, 2, 3$. Parameters: horizontal waveguide thickness $h = 0.2\,\mu\mathrm{m}$, TE polarized waves at a vacuum wavelength of $1.55\,\mu\mathrm{m}$, refractive indices $n_{\mathrm{g}} = 3.4$ (cores) and $n_{\mathrm{b}} = 1.45$ (background). [27]

Here $\psi^{\cdot}_{\cdot}$ are mode profiles of the form (1.2) (with the role of the coordinate axes exchanged, where necessary). Superscripts f,b identify the forward or backward propagating versions of the mode of the horizontal core, while superscripts u, d and the subscript m denote the upward or downward travelling m-th order modes of the vertical waveguide. The unknown amplitudes $f(z)$, $b(z)$ and $u_m(x)$, $d_m(x)$ associated with the modes of the horizontal and vertical channels are functions of their respective natural propagation coordinates x and z.

We apply the formalism of Section 1.2 with these amplitudes discretized on FE meshes that cover the intervals $z \in [v/2 - 1.5\,\mu\mathrm{m}, v/2 + 1.5\,\mu\mathrm{m}]$ and $x \in [w/2 - 1.5\,\mu\mathrm{m}, w/2 + 1.5\,\mu\mathrm{m}]$ with stepsizes $\Delta x = \Delta z = 0.025\,\mu\mathrm{m}$. The integrals (1.18) are evaluated over the computational window $x, z \in [-4, 4]\,\mu\mathrm{m}$. Initial amplitudes $|f(z_{\mathrm{l}})| = 1$, $b(z_{\mathrm{r}}) = u_m(x_{\mathrm{b}}) = d_m(x_{\mathrm{t}}) = 0$ at the FE-interval boundaries z_{l}, z_{r}, x_{b}, x_{t} specify an excitation of the structure from the left by the forward mode of the horizontal channel.

Figure 1.7 compares the present HCMT results with reference values, obtained by a rigorous quasi-analytical technique (QUEP, [40]), for crossings with different vertical core width v. The oscillatory behaviour can be attributed to additional guided modes that are supported by the vertical core with growing v. The agreement between the HCMT and QUEP data appears reasonable, given the simplicity of the template (1.26). This template comprises lossless guided modes only. Since no loss

mechanism of any kind is built in, the HCMT scheme is power conservative, at least on the scale of the figure. (The power balance can actually serve as an indicator of convergence.)

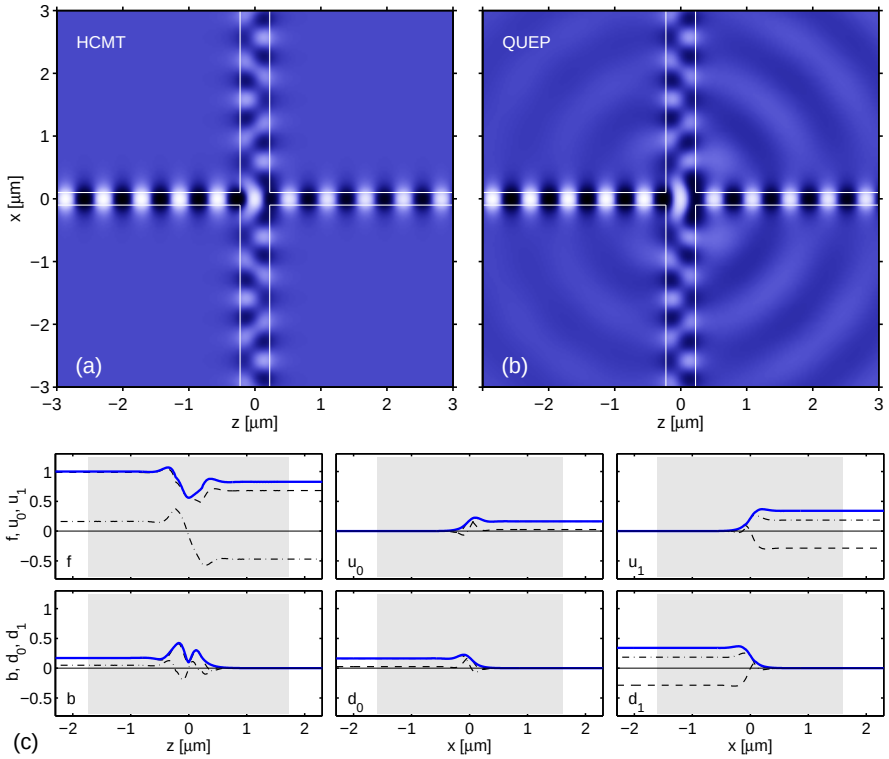

Fig. 1.8. For the crossing of Figure 1.7 with $v = 0.45\,\mu$m: Field plots (a, b), time snapshots of the principal component E_y of the TE fields, HCMT simulation (a), and QUEP result (b, [40], reference). Panels (c) show the amplitude functions f, b of the right- and left-travelling fundamental modes in the horizontal channel (first column), and functions u_m, d_m of the upward and downward propagating modes of order $m = 0, 1$ of the vertical channel (second and third columns); real parts (dashed), imaginary parts (dash-dotted), and absolute values (continuous lines) of the complex valued functions. [27]

Figure 1.8 collects results for the crossing with vertical core width $v = 0.45\,\mu$m. With the exception of the missing radiative part, the HCMT field (a) covers adequately the guided wave features of the reference field (QUEP, b). Although no direct analytical expressions are available, the HCMT technique still permits one to inspect the mode evolutions, e.g. it allows one to identify a central region of strong guided wave interaction, by examining the individual numerically represented modal

amplitudes[7]. Figure 1.8(c) shows their dependence on the respective propagation coordinates.

1.3.4 Microresonators with circular cavities

For more than a decade, circuits of integrated optical micro-ring or -disk resonators have been intensely investigated [44, 45], where modelling techniques of CMT-type are frequently seen. We test the HCMT technique with the single-cavity filter of Figure 1.9, for a parameter set adopted from [46] (dimensions are transferred to the spectral region around $1.56\,\mu$m). In line with most other modelling approaches we restrict the analysis to unidirectional wave propagation.

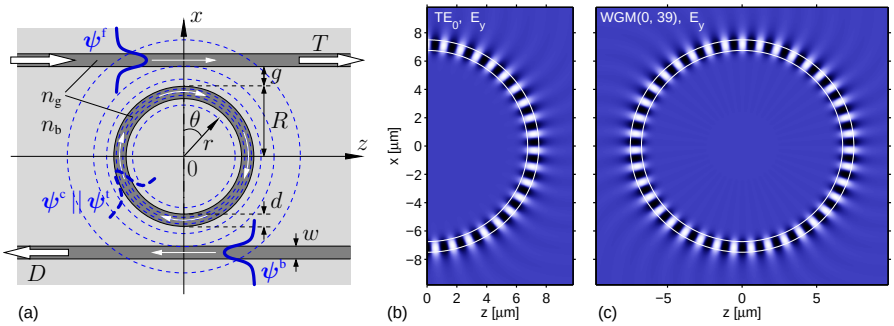

Fig. 1.9. A micro-ring filter with a circular cavity, evanescently coupled to two parallel straight bus waveguides (a). Cartesian coordinates x, z and polar coordinates r, θ apply. Parameters: refractive indices $n_\mathrm{b} = 1.0$ (background), $n_\mathrm{g} = 1.5$ (guiding regions), bus waveguides, core width $w = 0.6\,\mu$m, gaps $g = 0.3\,\mu$m, cavity radius $R = 7.5\,\mu$m, core width $d = 0.75\,\mu$m. TE waves from a spectral region around the target wavelength $\lambda \approx 1.56\,\mu$m are considered. Bend modes $\boldsymbol{\psi}^\mathrm{t}$ (b) or alternatively whispering-gallery resonances $\boldsymbol{\psi}^\mathrm{c}$ (c) contribute to the HCMT template in the cavity region. Fields for a fundamental bend mode with complex propagation constant $\gamma/k = 1.294 - \mathrm{i}6.5 \cdot 10^{-6}$ (b) and a WGM of radial order 0 and angular order 39, with resonance wavelength $\lambda_\mathrm{r} = 1.5637\,\mu$m and quality-factor $Q = 1.1 \cdot 10^5$ (c) are shown. [29, 30]

At the target wavelength, the cavity ring supports low-loss bend modes of fundamental radial order only. Using the ingredients as discussed in Section 1.2, and implying the relations $r(x,z)$, $\theta(x,z)$ between polar and Cartesian coordinates, one readily writes the following template for the filter device:

$$\begin{pmatrix} \boldsymbol{E} \\ \boldsymbol{H} \end{pmatrix}(x,z) = f(z)\,\boldsymbol{\psi}^\mathrm{f}(x,z) + b(z)\,\boldsymbol{\psi}^\mathrm{b}(x,z) + t(\theta)\,\boldsymbol{\psi}^\mathrm{t}(r,\theta), \tag{1.27}$$

[7] The overall phase of the solution has been adjusted to exhibit the maximum amplitude of the standing waves in the field plots Figure 1.8(a, b), therefore $f(z_\mathrm{l})$ differs from 1.

Here $\boldsymbol{\psi}^{\mathrm{f}}$, $\boldsymbol{\psi}^{\mathrm{b}}$, and $\boldsymbol{\psi}^{\mathrm{t}}$ are given basis fields of the forms (1.2) and (1.7), associated with the forward propagating mode of the upper channel, with the backward propagating mode of the lower channel, and with the bend mode that circles the cavity. These are superimposed with amplitude functions f, b, and t, our primary unknowns.

Alternatively we can model the cavity field in terms of whispering gallery modes (WGMs). The part of the template that relates to the straight waveguides remains as before. We add the WGMs supported by the cavity that might become relevant in the wavelength range of interest. The template then reads:

$$\begin{pmatrix} \boldsymbol{E} \\ \boldsymbol{H} \end{pmatrix}(x,z) = f(z)\,\boldsymbol{\psi}^{\mathrm{f}}(x,z) + b(z)\,\boldsymbol{\psi}^{\mathrm{b}}(x,z) + \sum_j c_j\,\boldsymbol{\psi}^{\mathrm{c}}_j(r,\theta), \tag{1.28}$$

Here $\boldsymbol{\psi}^{\mathrm{c}}_j$ are the resonant field profiles (1.11) of different radial and angular order, superimposed with — at present unknown — coefficients c_j. We apply the HCMT formalism with f and b discretized on the interval $z \in [-10, 10]$ with a stepsize of $\Delta z = 0.1\,\mu\mathrm{m}$, and, in case of the bend mode template (1.27), t discretized on the interval $\theta \in [0, 2\pi]$ with a stepsize $\Delta z/R$. WGMs of fundamental radial order, and of angular order 37–41 are taken into account for template (1.28). The resulting systems of linear equations (1.20) are of dimensions 873 (bend modes) and 407 (WGMs), respectively, in both cases with two given initial values.

Figure 1.10(a) compares results from both models, with rigorous numerical data obtained by external solvers. Each transmission resonance can be associated with a WGM that contributes the strongest to the overall field at the respective wavelength. One observes an excellent agreement of the two HCMT models, with the numerical reference data, and also with results from a traditional, differential equation based, CMT approach [46]. This latter model splits the resonator into two coupler regions, each with close-by bend and straight waveguide segments, and embeds the coupler scattering matrices obtained as the solution of CMT equations in an analytic resonator description.

Figures 1.11 shows an example of a resonant field pattern generated with the bend mode HCMT model. Waves propagate clockwise, following external input in the top left port. The slightly larger intensity in the right half of the cavity, and the levels of off-resonance power drop Figure 1.10, hint at a certain amount of non-resonant power transfer, from the upper to the lower bus waveguide. Hence this must be considered a strongly coupled configuration.

Inspection of the modal amplitudes in panels (b)–(d) of Figure 1.11 quantifies the wave interaction in the regions of closest approach around $z = 0$ and $\theta = 0, \pi$. Note that this concerns overlaps of non-orthogonal fields; values of f and b above 1 are physically possible. Outside the interaction regions the level $|t|$ appears to be constant; whilst included in the basis field, the attenuation of the bend mode is not visible on the scale of the figure. The slight slope of $\mathrm{Re}\,t$ and $\mathrm{Im}\,t$ compensates for the replacement $\gamma \to \kappa$ as explained in Section 1.2.2.

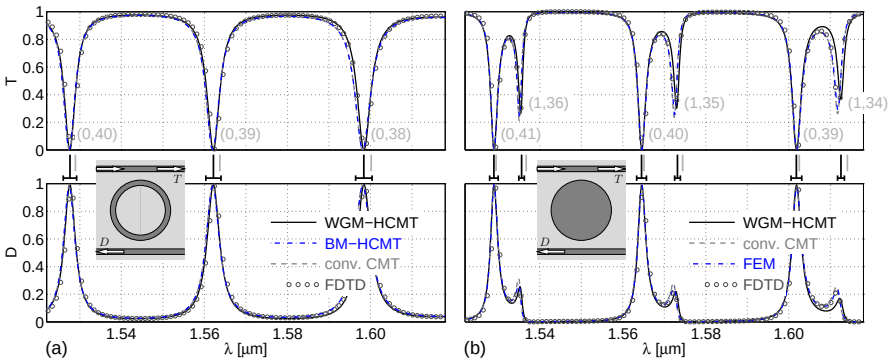

Fig. 1.10. Spectral properties of micro-ring (a) and -disk (b) resonators, with the parameters of Figure 1.9 (disk: material with refractive index n_g fills the ring interior); transmitted and dropped optical power T, D as a function of the excitation wavelength λ. The plots compare results of different methods. *WGM-HCMT* (continuous) and *BM-HCMT* (dash-dotted, (a) only): HCMT results [29, 30] with templates (1.28) and (1.27), respectively. *conv. CMT* (dashed): conventional CMT [46], *FEM* (dash-dotted, (b) only): commercial finite element solver [24, 30]. *FDTD* (markers): finite-difference-time-domain, commercial [23, 30]. The labels given for the resonances refer to the dominant contributing WGM. The marker lines between the T- and D-panels are positioned at the resonance wavelengths of the separate WGMs (light grey), and of the HCMT supermodes (black); the lower bars indicate the supermode linewidths. [29, 30]

A single WGM as in Figure 1.9, with its rotationally constant power distribution, leads to exactly the same intensity levels on both sides of the cavity [30]. Our HCMT model, however, includes several nearby WGMs as well. According to part (b) of Figure 1.12, although each WGM is clearly excited the strongest at wavelengths close to its own resonance wavelength, their amplitudes are not quite zero at the positions of other resonances close-by. These small contributions suffice to realize the resonant field shown in Figure 1.12(a), with the slight difference in intensity for $\pm z$, as observed already in Figure 1.11(a). Apparently, the field imbalance can alternatively be attributed to the interference of neighbouring WGMs.

Part (b) of Figure 1.10 refers to a device with parameters of Figure 1.9, but with the interior of the ring filled with the high-index medium. The disk cavity then supports, in the frequency range in question, WGMs of fundamental and first radial order. Our HCMT template (1.28) includes WGMs $(0, 37)$–$(0, 43)$ and $(1, 32)$–$(1, 38)$; the transmission resonances in Figure 1.10(b) are labelled accordingly. We still observe a satisfying agreement with the numerical reference data, with moderately larger deviations at the positions of the first order WGMs. This could be attributed to the the larger radial extent of the WGM$(1, .)$ fields, leading to a stronger overlap with the straight cores, i.e. to a global field approximation with more pronounced violation of Eqs. (1.1).

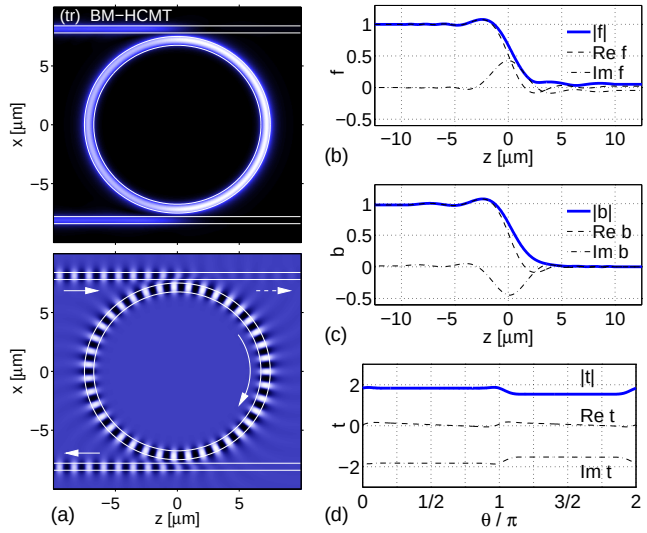

Fig. 1.11. For the micro-ring filter of Figure 1.10(a), bend mode based model: resonance at $\lambda = 1.5621$ µm. (a): Field pattern, physical time snapshot and field modulus, principal electric component E_y of the TE waves. (b)–(d): Coupled mode amplitudes, functions $f(z)$, $b(z)$, and $t(\theta)$ associated with the forward waves in the upper channel, with the backward waves in the lower channel, and with the cavity bend mode. [29, 30]

When compared to the ring, the curved interface of the disk supports radially fundamental WGMs of slightly higher quality (the higher interior refractive index "pulls" the field inwards). One thus observes transmission resonances with narrower linewidths. But note that here the interaction between bus waveguides and WGMs dominates: the WGMs of fundamental radial order interact more efficiently with the waves in the bus cores, hence they appear with wider transmission peaks than the WGMs of first radial order, which are originally of lower quality.

While so far we have discussed the spectral properties merely on the basis of the wavelengths scans of the transmission, the supermode analysis according to Section 1.2.7 permits similar conclusions. Respective results are indicated by the markers above the D panels of Figure 1.10(a, b). Although each WGM (grey lines) can be associated, by means of proximity of resonance wavelength, with one of the transmission resonances, there is some noticeable deviation in the peak positions. Further, the linewidth associated with the individual WGMs is much smaller than the widths of the transmission peaks (cf. [30] for tabulated values). This is rectified by the supermode analysis: Based on a template (1.28) that covers WGMs as well as the (here unidirectional) power outlets through the straight channels, the supermodes exhibit resonance wavelengths and linewidths that adequately predict the blue-shifted positions and widths of the transmission peaks.

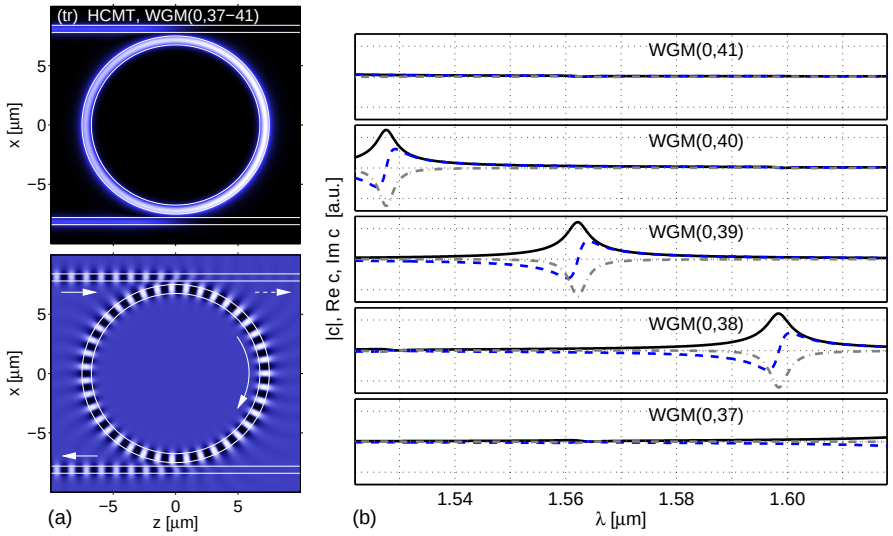

Fig. 1.12. WGM-HCMT model of the micro-ring filter of Figure 1.10(a), field (time snapshot and field modulus, E_y) at a resonance wavelength $\lambda = 1.5622\,\mu$m (a), and spectral behaviour of the HCMT amplitudes c_j associated with the individual whispering gallery resonances. The simulations take the WGMs(0, 37–41) into account. [30]

1.3.5 A 3-ring photonic molecule, excited by a straight waveguide

For our last example we consider an arrangement of three of the cavity rings from Section 1.3.4, as shown in the schematics of Figure 1.13. The rings are positioned at the corners of an equilateral triangle, such that the structure is vertically symmetric with respect to the central horizontal axis. A single vertical straight bus waveguide is placed close to the leftmost ring. Configurations of this type can function as resonant mirrors / reflectors, as predicted by the parametric scattering-matrix model of [47, 48]. One might view the structure as a photonic "molecule" (if the bus channel is omitted), constituted by the three rings as photonic "atoms". Ref. [49] provides a rigorous integral equation analysis of isolated molecules with emphasis on their Q-factors (but note that the present example concerns "large" rings, with WGM resonances of high angular order, with the excitation through the bus waveguide taken into account). Further recent studies include a parametric pathway analysis, aiming at an application as a sensor [50], and experimental observations [51], motivated by an approximate analytical WGM based description [52]. In this section we will discuss the respective HCMT results [29,30], again using alternatively the bend mode or WGM based models for the fields associated with the cavities. Observe that, for this example, a conventional scattering matrix model, which would require a division of the structure into separate coupling regions, with well defined connecting waveguide ports, seems to be neither appropriate nor convenient.

Obviously, in contrast to Section 1.3.4, a bidirectional model is essentially required. Suitable templates are formally similar to (1.27) and (1.28): f and b then refer to the directional, here up- and downward travelling guided modes of the single bus channel. Contributions related to clockwise and anticlockwise propagating bend modes [31], or alternatively clockwise and anticlockwise rotating whispering gallery resonances [30], need to be included for each of the three rings. Our bend mode and WGM based HCMT models predict the spectral transmission properties of Figure 1.13.

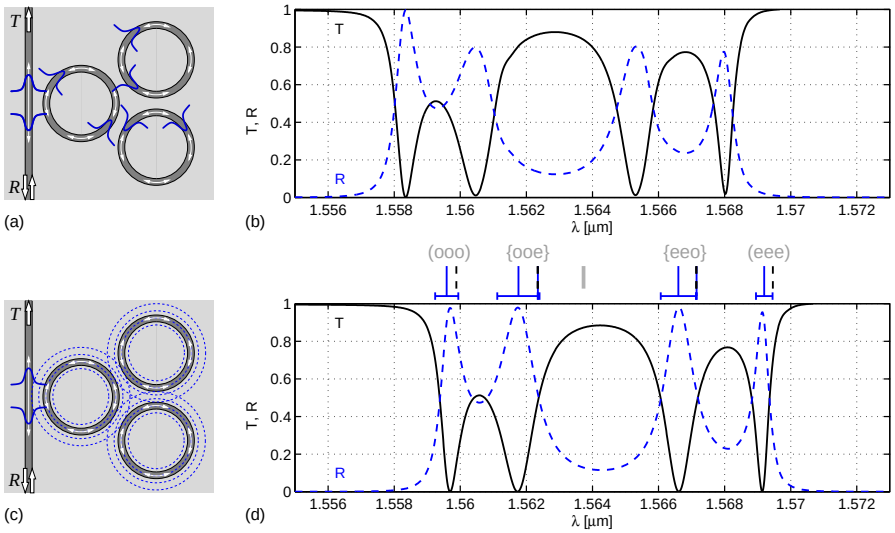

Fig. 1.13. A triangular arrangement of coupled rings, accessed by a single bus waveguide. Parameters are as in Figure 1.9, with equal gaps g between the cores at the points of closest approach. TE waves are considered. Transmittance T and reflectance R versus the excitation wavelength λ, evaluated with the bend mode based HCMT model (a, b) [29], and with a WGM based HCMT template (c, d) [30]. The markers above panel (d) indicate the resonance WGM(0, 39) of an individual ring (single light grey line), the HCMT supermodes (dashed) of the three-ring molecule, without the bus waveguide (cf. Figure 1.14 for the classification of resonances), and the supermodes for the entire compound of molecule and waveguide (continuous, with the associated linewidths).

We look at the spectral region close to the WGM(0, $\pm$39) resonance of a single ring. The features of Figure 1.13 cover a total wavelength range of about 10 nm, which is roughly a quarter of the free spectral range of the individual rings. One can expect that the shapes repeat at the positions of neighbouring resonances in Figure 1.10, then with dominant WGMs of different angular order.

The HCMT models differ significantly in the numbers of unknowns that are introduced to represent the field of the cavities. For the bend mode based model, each amplitude function t is discretized on the interval $\theta \in [0, 2\pi]$ with a stepsize of

$0.4\,\mu\text{m}/R$. Six amplitude functions are required, one for each of two directional bend modes of each ring; hence the field of the three cavities is represented with 708 unknowns. In contrast, for the WGM based template, only 6 coefficients are introduced in total for the two directional WGMs of each ring. Consequently, it comes as no surprise that also the results differ, most notably in the positions of the resonance peaks and in the extremal reflectance levels, for the three right-most peaks. Still, the general spectral features are adequately captured by the much simpler WGM model.

We might thus seek to interpret the resonant features of the transmission spectrum with the help of the WGM model. To this end we regard the three rings, without the bus waveguide, as one composite cavity. One expects that, in the present range of frequencies, the properties of this molecule, are given by the interaction of the WGMs$(0, \pm 39)$ associated with the three ring atoms. Hence we use a HCMT template that consists of the six WGMs only. The procedure for supermode analysis of Section 1.2.7 then predicts the six eigenfields of Figure 1.14, associated with the resonance wavelengths marked in Figure 1.13.

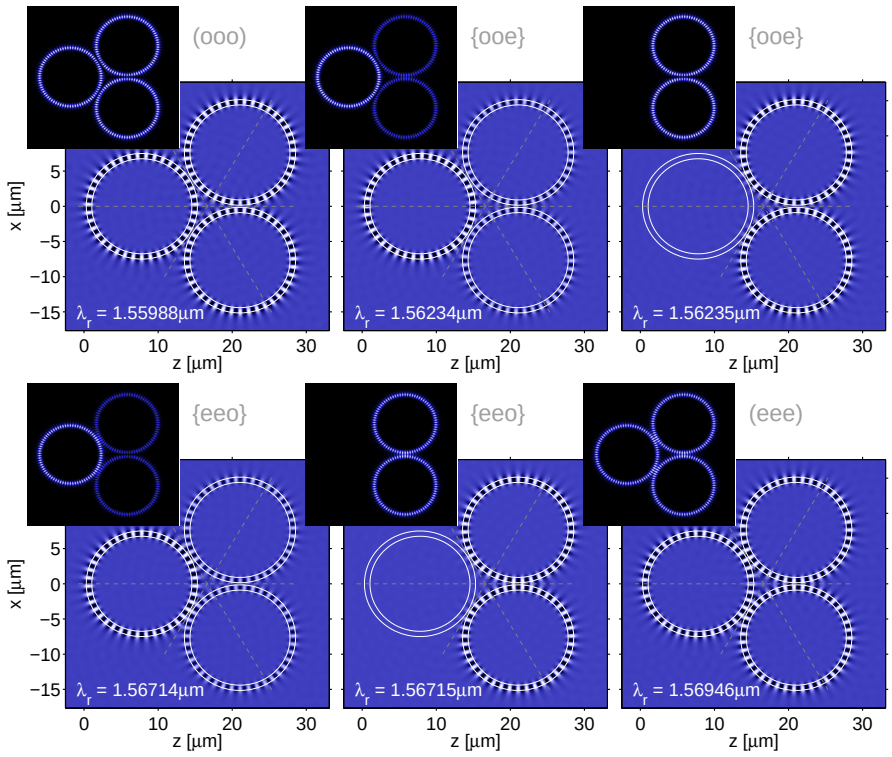

Fig. 1.14. Supermode profiles of the three-ring molecule, time-snapshots of the standing wave pattern (large panels) and absolute values (smaller insets) of the principal electric field component. [30]

Purely standing waves (angular direction) are observed in all cavities, realized by clockwise and anticlockwise rotating WGMs with amplitudes of equal magnitude. The triangular structure is mirror-symmetric with respect to the three axes hinted at by the thin dashed lines in the field plots. This implies modes with even (e) or odd parity (o) with respect to each of these axes. Respective labels are given for the panels in Figure 1.14 and the resonance wavelengths in Figure 1.13. One finds a "fundamental" supermode (eee) with the longest resonance wavelength / lowest energy that exhibits the least "strained" profile, i.e. a field that is symmetric across all three lines, and thus exhibits the lowest curvature. Likewise the supermode (ooo) with the most "strained" field appears at the shortest wavelength, or at highest energy, respectively. Further there are two pairs of supermodes, each pair twofold degenerate[8]. Symmetry properties can also be discussed for these [30]; Figure 1.14 shows, however, that one of these modes in each pair appears with only very small relative field levels in the leftmost cavity.

If one now places the bus channel next to the compound, the incoming waves interact only with those molecule supermodes that exhibit non-negligible field overlaps with the bus core. Hence the transmission spectra show only four peaks, not six. Given the specific type of excitation, the supermodes in the third and fifth panels behave as nonradiative, "dark" states. In our present model they are degenerate with the radiating "bright" states of panels two and four. Other types of illumination, or some small perturbation, might thus produce resonance features of Fano-type [53], here for a comparably large purely dielectric model system.

1.4 HCMT in 3-D

The formalism as outlined in Section 1.2, as well as the prototypes for field templates given with the examples, should also be valid directly for 3-D configurations. The basis fields in the template (1.13) then depend on three coordinates; integrals in Eq. (1.14) and subsequent expressions need to cover the respective 3-D computational window. The list of expected challenges and issues, as far as it can be predicted at this stage, includes:

- For the existing 2-D implementation we can rely on analytical or quasi-analytical basis fields, and the respective solvers are directly embedded into the HCMT programs. Contrarily, the 3-D approach requires modes of straight and bend waveguides with 2-D cross sections, and resonant profiles of 3-D cavities, as basis fields. Depending on the complexity of the structures, and on the desired approximation level, already the computation of these basis fields must be considered a non-trivial task. Although respective modules are commercially available, some

[8] The computational setting, with, e.g. the rectangular computational window, and quadrature rules applied subsequently along the x- and z-coordinates, does not respect the triangular symmetry, i.e. must be expected to numerically lift the degeneracy.

non-negligible effort to realize workable interfacing with the HCMT programs is to be expected. In particular, some effort will be necessary to operate the "external" mode solvers in an automated way, avoiding case-dependent user interaction (e.g. for specifying initial guesses, or limits, for eigenvalues, or to select useful modes from a batch of numerical eigenfields) as far as possible.

- While the final step in the computations, the solution of the (small scale) systems (1.22), (1.24) should be cheap, the setup of the respective matrices, i.e. the evaluation of the modal element overlaps (1.18), will be the largest computational burden. Ways for efficient integration of the products of the numerically represented basis fields will have to be found and implemented, using e.g. suitable interpolation techniques, avoiding redundancy, exploiting specifics of the mode solvers, making use of the *a-priori* restricted computational domain of the eigenfields, etc.. When employing higher order procedures for numerical quadrature, discontinuities of certain field components, or of their derivatives, at interfaces between different media will have to be taken into account. (We have observed respective effects already in the 2-D implementation.) Note that, for comparable circuits and field templates, the number of actual unknowns *will be the same* in the 2-D and the 3-D setting. Realizing this extremely favorable scaling behaviour will probably the biggest challenge for the 3-D implementation.
- Considering the variational character of the HCMT scheme [27], we expect that (even numerically) "exact" solutions to the eigenmode problems for the constituents (channels, cavities) of the structures, will not always be strictly necessary. The programs will be prepared to digest also approximate basis fields, e.g. merely semivectorial modes [54, 55] of channel waveguides. The variational / perturbational nature of the technique can be expected to compensate to a certain extent for errors in the field template. This feature might ease the two former issues in specific cases.

1.5 Concluding remarks

Obviously, with the major ingredient being a "reasonable" trial field, the HCMT approach, as discussed here, necessarily relies to a large extent on physical or engineering intuition. The method then allows one to quantify the intuitive description of the internal workings of the optical circuits; it provides an implementation of the way that these devices are commonly discussed.

Adopting, for a given structure, a physically plausible field template of the form (1.3), (1.8), (1.12), or (1.13), respectively, constitutes the major approximation. Starting with the frequency domain Maxwell equations, once this template has been fixed, no further heuristics are required to arrive at the desired approximate solutions for the optical field, irrespective of the specifics of the structure under investigation.

The template (1.13) is of a form that, in principle, also covers rigorous numerical discretizations of the optical fields. Hence this may be viewed as a numerical finite ele-

ment (FE) technique with highly specialized, structure-adapted elements (the above "modal elements"). When refining the FE approximations (1.5), *convergence* can obviously only be expected up to approximations of the actual solutions of Eqs. (1.1) in the form of Eqs. (1.3), (1.8), (1.12), with *continuous* amplitude functions.

Emphasis here is on approximations with very few unknowns, when compared to standard 2- or 3-D FE settings. As much as possible of the physics is already built into the modal elements, leading to small or merely moderate sized algebraic systems (1.21) or (1.24). For the examples in Section 1.3, typical numbers of unknowns range from less than ten (supermodes of the photonic molecule without bus channel, expressed through selected WGMs of the individual cavities) to a few hundreds (amplitude functions for straight and bend channels, discretized by 1-D FEs). Note that the dimension of these systems scales with the *lengths* of the channels / with the number of resonances, rather than with the *area* (2-D) or *volume* (3-D) of the computational window required to cover the circuits, as in conventional finite element or finite difference schemes.

So far we've been interested in approximate solutions of the homogeneous system (1.1), subject to boundary conditions that accommodate the prescribed incoming (guided) waves, together with arbitrary outgoing waves. (Cf. e.g. [56, 57] or the appendix of [27] for more formal statements.) While these boundary conditions do not show up anywhere explicitly in the present formalism, they are built into the template (1.13) through the appropriate selection of contributing fields.

An alternative "true variational" derivation the formalism [27] starts with a functional representation of the Maxwell curl equations in the frequency domain (1.1), with additional terms that realize the necessary transparent-influx boundary conditions. Variational restriction [1,58] of that functional to the field template (1.13) then permits one to establish an algebraic system of equations for the discretized amplitude functions, which differs from Eqs. (1.17) or (1.21). While the comparison gives virtually identical results for the examples considered, the present scheme obtained with the Galerkin projection has certain practical advantages [27].

Provided that the basic approximation remains valid, i.e. provided the initial field template remains appropriate, the supplied basis fields need not necessarily be exact solutions even for parts of the configuration. This might open up ways to conveniently estimate the consequences of all kinds of "small" effects, changes to the permittivity, on the transmission or resonance characteristics of a device. One would compute basis fields for the channels of a simpler, "unperturbed", original structure, then solve the system with the "perturbed", modified permittivity in Eq. (1.14), or for a series of these perturbations. The variational trait of the HCMT formalism provides perturbation theory "for free". So far we have only taken a peek at the manifold of possible applications: Ref. [30] shows an example where an HCMT supermode computation (cf. Section 1.2.7) for a field template with single whispering gallery modes permits one to evaluate the influence of a change in the core refractive index of underlying ring cavity on the resonance wavelengths. In that case one can even state an explicit analytical expression for the perturbation.

As is common to all CMT variants, beyond certain consistency checks (e.g. the power balance, reciprocity properties), there is usually no direct possibility for assessing the accuracy of the simulations. There is no strict guarantee that the approach works in other regimes of parameters even for the given examples. Still, the examples considered so far show that the HCMT models adequately cover a range of interesting structures. Where possible (in particular in 2-D, frequently only with unacceptable numerical effort — or not at all — in 3-D), benchmarking versus numerical simulations, typically at random for characteristic configurations, can give clues as to how far the approximate HCMT models can be trusted.

Acknowledgments

Financial support from the German Research Foundation (Deutsche Forschungsgemeinschaft DFG, projects HA 7314/1-1 and TRR 142) is gratefully acknowledged.

References

1. C. Vassallo. *Optical Waveguide Concepts*. Elsevier, Amsterdam, 1991.
2. S. L. Chuang. A coupled mode formulation by reciprocity and a variational principle. *Journal of Lightwave Technology*, 5(1):5–15, 1987.
3. W. P. Huang. Coupled mode theory for optical waveguides: an overview. *Journal of the Optical Society of America A*, 11(3):963–983, 1994.
4. D. G. Hall and B. J. Thompson, editors. *Selected Papers on Coupled-Mode Theory in Guided-Wave Optics*, volume MS 84 of *SPIE Milestone Series*. SPIE Optical Engineering Press, Bellingham, Washington USA, 1993.
5. A. W. Snyder and J. D. Love. *Optical Waveguide Theory*. Chapman and Hall, London, New York, 1983.
6. R. März. *Integrated Optics — Design and Modeling*. Artech House, Boston, London, 1994.
7. K. Okamoto. *Fundamentals of Optical Waveguides*. Academic Press, SanDiego, 2000.
8. D. R. Rowland and J. D. Love. Evanescent wave coupling of whispering gallery modes of a dielectric cylinder. *IEE Proceedings, Pt. J*, 140(3):177–188, 1993.
9. K. R. Hiremath and M. Hammer. Circular integrated optical microresonators: Analytical methods and computational aspects. In I. Chremmos, N. Uzunoglu, and O. Schwelb, editors, *Photonic Microresonator Research and Applications*, Springer Series in Optical Sciences, Vol. 156, pages 29–59. Springer, London, 2010.
10. B. E. Little, S. T. Chu, H. A. Haus, J. Foresi, and J.-P. Laine. Microring resonator channel dropping filters. *Journal of Lightwave Technology*, 15(6):998–1005, 1997.
11. C. Manolatou, M. J. Khan, S. Fan, P. R. Villeneuve, H. A. Haus, and J. D. Joannopoulos. Coupling of modes analysis of resonant channel add-drop filters. *IEEE Journal of Quantum Electronics*, 35(9):1322–1331, 1999.
12. M. J. Khan, C. Manolatou, S. Fan, P. R. Villeneuve, H. A. Haus, and J. D. Joannopoulos. Mode-coupling analysis of multipole symmetric resonant add/drop filters. *IEEE Journal of Quantum Electronics*, 35(10):1451–1460, 1999.

13. S. Fan, P. R. Villeneuve, J. D. Joannopoulos, M. J. Khan, C. Manolatou, and H. A. Haus. Theoretical analysis of channel drop tunneling processes. *Physical Review B*, 59(24):15882–15892, 1999.
14. Q. Li, T. Wang, Y. Su, M. Yan, and M. Qiu. Coupled mode theory analysis of mode-splitting in coupled cavity system. *Optics Express*, 18(8):8367–8382, 2010.
15. M. Lohmeyer, N. Bahlmann, O. Zhuromskyy, and P. Hertel. Radiatively coupled waveguide polarization splitter simulated by wave-matching based coupled mode theory. *Optical and Quantum Electronics*, 31:877–891, 1999.
16. M. Lohmeyer, N. Bahlmann, O. Zhuromskyy, H. Dötsch, and P. Hertel. Phase-matched rectangular magnetooptic waveguides for applications in integrated optics isolators: numerical assessment. *Optics Communications*, 158:189–200, 1998.
17. M. Lohmeyer, N. Bahlmann, O. Zhuromskyy, H. Dötsch, and P. Hertel. Unidirectional magnetooptic polarization converters. *Journal of Lightwave Technology*, 17(12):2605–2611, 1999.
18. P. E. Barclay, K. Srinivasan, and O. Painter. Design of photonic crsytal waveguides for evanescent coupling to optical fiber tapers and integration with high-Q cavities. *Journal of the Optical Society of America B*, 20(11):2274–2284, 2003.
19. P. E. Barclay, K. Srinivasan, M. Borselli, and O. Painter. Efficient input and output fiber coupling to a photonic crystal waveguide. *Optics Letters*, 29(7):697–699, 2004.
20. R. Stoffer, K. R. Hiremath, M. Hammer, L. Prkna, and J. Čtyroký. Cylindrical integrated optical microresonators: Modeling by 3-D vectorial frequency domain coupled mode theory. *Optics Communications*, 256(1–3):46–67, 2005.
21. C. Vassallo. 1993-1995 Optical mode solvers. *Optical and Quantum Electronics*, 29:95–114, 1997.
22. P. Bienstmann, S. Selleri, L. Rosa, H. P. Uranus, W. C. L. Hopman, R. Costa, A. Melloni, L. C. Andreani, J. P. Hugonin, P. Lalanne, D. Pinto, S. S. A. Obayya, M. Dems, and K. Panajotov. Modelling leaky photonic wires: a mode solver comparison. *Optical and Quantum Electronics*, 38(9–11):731–759, 2006.
23. PhoeniX Software, Enschede, The Netherlands; http://www.phoenixbv.com.
24. JCMwave GmbH, Berlin, Germany; http://www.jcmwave.com.
25. Lumerical Solutions, Inc., Vancouver, Canada; http://www.lumerical.com.
26. Photon Design, Oxford, United Kingdom; http://www.photond.com.
27. M. Hammer. Hybrid analytical / numerical coupled-mode modeling of guided wave devices. *Journal of Lightwave Technology*, 25(9):2287–2298, 2007.
28. M. Hammer. Chains of coupled square dielectric optical microcavities. *Optical and Quantum Electronics*, 40(11–12):821–835, 2009.
29. M. Hammer. HCMT models of optical microring-resonator circuits. *Journal of the Optical Society of America B*, 27(11):2237–2246, 2010.
30. E.F. Franchimon, K.R. Hiremath, R. Stoffer, and M. Hammer. Interaction of whispering gallery modes in integrated optical micro-ring or -disk circuits: Hybrid CMT model. *Journal of the Optical Society of America B*, 30(4):1048–1057, 2013.
31. K. R. Hiremath, M. Hammer, R. Stoffer, L. Prkna, and J. Čtyroký. Analytical approach to dielectric optical bent slab waveguides. *Optical and Quantum Electronics*, 37(1-3):37–61, 2005.
32. L. Prkna, J. Čtyroký, and M. Hubálek. Ring microresonator as a photonic structure with complex eigenfrequency. *Optical and Quantum Electronics*, 36(1/3):259–269, 2004.
33. J. D. Jackson. *Classical Electrodynamics, 3rd. ed.* Wiley, New York, 1998.
34. M. A. Popović, C. Manolatou, and M. R. Watts. Coupling-induced resonance frequency shifts in coupled dielectric multi-cavity filters. *Optics Express*, 14(3):1208–1222, 2006.

35. M. Maksimovic, M. Hammer, and E. van Groesen. Field representation for optical defect microcavities in multilayer structures using quasi-normal modes. *Optics Communications*, 281(6):1401–1411, 2008.
36. M. Maksimovic, M. Hammer, and E. van Groesen. Coupled optical defect microcavities in 1d photonic crystals and quasi-normal modes. *Optical Engineering*, 47(11):114601 1–12, 2008.
37. M. Maksimovic. *Optical resonances in multilayer structures*. University of Twente, Enschede, The Netherlands, 2008. Ph.D. Thesis.
38. M. Hammer. METRIC — Mode expansion tools for 2D rectangular integrated optical circuits. http://metric.computational-photonics.eu/.
39. K. R. Hiremath. CIRCURS — Circular resonator simulator. http://home.iitj.ac.in/∼k.r.hiremath/circurs/.
40. M. Hammer. Quadridirectional eigenmode expansion scheme for 2-D modeling of wave propagation in integrated optics. *Optics Communications*, 235(4–6):285–303, 2004.
41. W. H. Press, S. A. Teukolsky, W. T. Vetterling, and B. P. Flannery. *Numerical Recipes in C, 2nd ed.* Cambridge University Press, 1992.
42. M. Hammer. OMS — 1-D mode solver for dielectric multilayer slab waveguides. http://www.computational-photonics.eu/oms.html.
43. M. Lohmeyer and R. Stoffer. Integrated optical cross strip polarizer concept. *Optical and Quantum Electronics*, 33(4/5):413–431, 2001.
44. F. Michelotti, A. Driessen, and M. Bertolotti, editors. *Microresonators as building blocks for VLSI photonics*, volume 709 of AIP conference proceedings. American Institute of Physics, Melville, New York, 2004.
45. I. Chremmos, N. Uzunoglu, and O. Schwelb, editors. *Photonic Microresonator Research and Applications*. Springer Series in Optical Sciences, Vol. 156. Springer, London, 2010.
46. K. R. Hiremath, R. Stoffer, and M. Hammer. Modeling of circular integrated optical microresonators by 2-D frequency-domain coupled mode theory. *Optics Communications*, 257(2):277–297, 2006.
47. J. K. S. Poon, J. Scheuer, and A. Yariv. Wavelength-selective reflector based on a circular array of coupled microring resonators. *IEEE Photonics Technology Letters*, 16(5):1331–1333, 2004.
48. O. Schwelb and I. Chremmos. Band-limited microresonator reflectors and mirror structures. In I. Chremmos, N. Uzunoglu, and O. Schwelb, editors, *Photonic Microresonator Research and Applications*, Springer Series in Optical Sciences, Vol. 156, pages 139–163. Springer, London, 2010.
49. S. V. Boriskina. Theoretical prediction of a dramatic Q-factor enhancement and degeneracy removal of whispering gallery modes in symmetrical photonic molecules. *Optics Letters*, 31(3):338–340, 2006.
50. S. I. Schmid, K. Xia, and J. Evers. Pathway interference in a loop array of three coupled microresonators. *Physical Review A*, 84:013808, 2011.
51. C. Schmidt, M. Liebsch, A. Klein, N. Janunts, A. Chipouline, T. Käsebier, C. Etrich, F. Lederer, E.-B. Kley, A. Tünnermann, and T. Pertsch. Near-field mapping of optical eigenstates in coupled disk microresonators. *Physical Review A*, 85:033827, 2012.
52. C. Schmidt, A. Chipouline, T. Käsebier, E.-B. Kley, A. Tünnermann, and T. Pertsch. Observation of optical coupling in microdisk resonators. *Physical Review A*, 80:043841, 2009.
53. B. Gallinet and O. J. F. Martin. *Ab initio* theory of Fano resonances in plasmonic nanostructures and metamaterials. *Physcal Review B*, 83(23):235427, 2011.
54. M. S. Stern. Semivectorial polarised finite difference method for optical waveguides with arbitrary index profiles. *IEE Proceedings, Pt. J*, 135(1):56–63, 1988.

55. M. S. Stern. Semivectorial polarised H field solutions for dielectric waveguides with arbitrary index profiles. *IEE Proceedings, Pt. J*, 135(5):333–338, 1988.
56. B. Kettner. *Detection of Spurious Modes in Resonance Mode Computations — Pole Condition Method*. Freie Universität zu Berlin, Berlin, Germany, 2012. Dissertation.
57. L. Zschiedrich. *Transparent Boundary Conditions for Maxwells Equations: Numerical Concepts beyond the PML Method*. Freie Universität zu Berlin, Berlin, Germany, 2009. Dissertation.
58. E. W. C. van Groesen and J. Molenaar. *Continuum Modeling in the Physical Sciences*. SIAM publishers, Philadelphia, USA, 2007.